Journal of Applied Fluid Mechanics, Vol. 19, No. 1, pp. 3415-3428, 2026. Available online at www.jafmonline.net, ISSN 1735-3572, EISSN 1735-3645. https://doi.org/10.47176/jafm.19.1.3562



Peripheral Water Pressure Characteristics of Piers under Oblique Flow Conditions

Y. Li^{1,2}, Y. Y. Li¹, Q. Ma^{1,2†}, P. Y. Zhou¹, C. Z. Zhang¹, and X. S. Cheng¹

 Hehai College of Chongqing Jiaotong University, Chongqing, 400016, China
 Chongqing Southwest Research Institute for Water Transport Engineering, Chongqing Jiaotong University, Chongqing, 400016, China

[†]Corresponding Author Email: <u>maggie@cajtu.edu.cn</u>

ABSTRACT

To investigate the impact characteristics of oblique flow on dolphin-type pier structures in mountainous river confluence hubs, the Madao Hub of the Pinglu Canal—a pivotal component of China's Western Land-Sea New Corridor initiative-was examined in this study. Full-scale three-dimensional fluidstructure interaction (FSI) simulations were implemented, with validation against physical model experimental data. The flow characteristics and hydrodynamic pressure distributions around ship-berthing piers impacted by the tailwater flow from the Madao Hub were analyzed. Simulation results of the FSIs were benchmarked against standard empirical formulas. The results revealed that under the project's layout configuration, high-velocity flow propagated predominantly along the left bank, primarily impacting piers 8–10. The maximum positive pressure zone was located near the upstream corner of the most-affected berthing pier. As the flow traversed the pier's leading edge and impinged upon the sidewalls, the hydrodynamic pressure progressively attenuated, transitioning to negative values at the downstream end of the front face and upstream end of the side face. Comparisons indicated that the predicted values matched well with AS500 and IRS standards, whereas IRC 6 standard underestimated the hydrodynamic forces by 85%-90%. Therefore, the IRC 6 standard requires calibration to enhance its safety factor. This study elucidated the pressure distributions around piers under oblique flow conditions, providing a scientific foundation for structural layout optimization, pier geometry selection, and force analysis of piers near mountain river confluences.

Article History

Received April 3, 2025 Revised August 4, 2025 Accepted August 15, 2025 Available online November 5, 2025

Keywords:

Fluid-structure interaction Ship-berthing pier Oblique water flow Pressure characteristics Mathematical model

1. Introduction

The fluid-structure interaction (FSI) phenomenon with piers involves complex interplay between the water flow and the piers, and it is significant in bridge engineering, marine engineering, and hydraulic engineering. The forces exerted by water on piers influence the structural stability and can induce deformation, vibration, and fatigue. Previous studies on piers have primarily focused on the scour characteristics (Baduna Koçyiğit & Koçyiğit, 2024; Carnacina et al., 2019; Kadono et al., 2020), with limited research on the interactions between the water flow and piers. A comprehensive understanding of the hydrodynamic forces on pier surfaces is therefore crucial for designing, assessing, and optimizing bridges and related structures.

In recent years, substantial progress has been made in studying the water flow effects on piers. A numerical

method combining a high-order compact difference scheme and the immersed boundary method was used to simulate the flow around hyperbolic cylinders with varying aspect ratios and eccentricities. The vortexseparation point in the wake of the hyperbolic cylinders moved backwards compared to that of circular cylinders, reducing the drag coefficient by 27.6% (Luo et al., 2022). Based on simulations of flows past three circular cylinders in an equilateral-triangular configuration, five different flow regimes were identified. As the spacing ratio or Reynolds number increased, the wake flow threedimensionality intensified (Gao et al., 2019). Additionally, the large eddy simulation (LES) method was employed to analyze the three-dimensional flow around four-cylinder and five-cylinder arrays at Re = 3900 (Tu et al., 2020). A study on the turbulence characteristics in a dual-squarecylinder system indicated that reducing the cylinder spacing by 40% increased the vortex generation frequency by 25% (Rahman et al., 2022). Notably, rounded square cylinders were found to produce a flow pattern mutation when the dimensionless shear strength reached 0.4, providing insights for offshore structure design (Cao & Tamura, 2018).

Based on these findings on the section shapes and flow characteristics, structural optimization has become a key approach to enhance the engineering performance. Geometric modifications can significantly improve the structural stability. Increasing the fillet radius of rounded triangular cylinders was found to enhance the flow stability (Çelik & Altaç, 2023). Two-dimensional simulations indicated that the pier geometric parameters (shape and compression ratio) and the upstream flow velocity are key factors influencing the flow field characteristics, with compression effects leading to nonmonotonic velocity distributions and horseshoe vortex structures (Huang, 2023). Furthermore, bridge pier optimization using the finite volume method improved the flood resistance by 18% (Patil & Kadam, 2024a). These optimized designs not only enhance the structural performance but also provide more reliable models for subsequent FSI research.

To simulate FSI problems, computational fluid dynamics (CFD) simulations based on the finite element method (FEM) and the finite volume method (FVM) are commonly used (Baragamage & Wu, 2024; Jeong & Seong, 2014; Omara et al., 2023; Ozdemir et al., 2010; Sousa et al., 2024). These techniques effectively simulate the fluid and structural behaviors and their interactions. Compared to static models, dynamic FSI models better capture the true responses of piers, and it has been confirmed that the scour depth and flow velocity are key parameters in the scouring mechanism (Lin et al., 2022). Advances in numerical methods include the volume of fluid-FSI approach, which effectively simulates flood damage processes (Nan et al., 2023), and LES technology, which captures periodic oscillations of single-pile foundations (Zhao & Guo, 2024). Under seismic conditions, multi-component repair models improved the seismic response prediction accuracy by 22% (Pang et al., 2025). Large-scale single-pile foundation studies further quantified the coupling mechanisms between the water depth and the seismic wave spectra (Cai et al., 2025). A Poisson regression model demonstrated high reliability in predicting the pier water pressure (Patil & Kadam, 2024b). Hydrodynamic effects on underwater rectangular piers are critical for the seismic design of deep-water bridges (Chen et al., 2025), and the pier spacing and relative angles significantly influence multi-pier system coupling effects (Yang et al., 2020). A comparative study of international engineering standards revealed that computational results from simulations incorporating FSI effects were consistent with the standards, with Chinese standards tending to be conservative (Wang et al., 2015).

Despite these advancements, real-world engineering faces challenges due to complex oblique flows and a non-uniform water distribution, making the impact of water on piers even more intricate. Physical model tests can simulate various flow conditions; however, spatial and scale limitations hinder the accurate replication of the

turbulence, wave effects, and complex flow fields generated during ship berthing. At high flow velocities, local turbulence and vortices can form, creating asymmetric flow patterns that intensify the flow disturbances and local erosion. Oblique water flow can induce complex vortex structures, particularly at high velocities, where water may rotate around piers, forming asymmetric flow patterns that exacerbate uneven structural forces.

Given the complexity of the loading mechanisms on pier columns subjected to oblique hydrodynamic loading, a mathematical model of the three-dimensional FSIs was established in this study. Compared with conventional physical model tests, the proposed model significantly enhances the resolution of the dynamic flow-structure interplay processes, including flow separation and structural deformation, particularly for the frequently encountered yet insufficiently studied berthing dolphin configurations under oblique flow. High-resolution temporal sampling quantitatively resolved the asymmetric hydrodynamic pressure distribution and its evolution on the pier surfaces. Through fully coupled bidirectional computation of the hydrodynamic loads and structural dynamics, the model enables precise quantification of both the static pressure and vortex-induced vibration effects. Furthermore, it enables comprehensive flow field diagnostics and structural response metrics that can facilitate the optimization of specially configured berthing dolphin configurations to enhance the scour mitigation capacity, fatigue resistance, and structural integrity.

2. CASE STUDY

The Western Land-Sea New Passage Canal originates from the Pingtang River Estuary in Hengzhou City, Nanning. It crosses the watershed between the Shaping River and the Jiujiang tributary of the Qinzhou River, passes through Lulwu Town in Lingshan County, Qinzhou City, and follows the Qinzhou River southward before reaching the Qinzhou Port area in the Beibu Gulf. The Western Land-Sea New Passage Canal draws water from the main stream of the Xijiang River and the Xijin Reservoir. Spanning approximately 135 km, this canal serves as a key waterway linking inland rivers with the sea (see Fig. 1).

Under flood diversion conditions, the Madao Hub's spillway discharge channel intersects obliquely with the downstream navigation channel of the ship lock. This configuration causes the diverted flow to impact the leftside mooring area at an angle, generating intense turbulence and deteriorating flow conditions around the ship-berthing piers in this area (see Fig. 2). The presence of the piers obstructs the flow, creating a water level difference of approximately 2.0 m between the upstream and downstream sides, which negatively affects the pier stability. The turbulent spillway flow induces complex hydrodynamic effects, including boundary layer separation, vortex formation, and periodic vortex shedding around the pier structures. These phenomena result in pulsating pressures that can trigger structural vibrations, potentially compromising the stability and safety of the ship-berthing piers. This study examined the water pressure



Fig. 1 Pinglu Canal Basin map

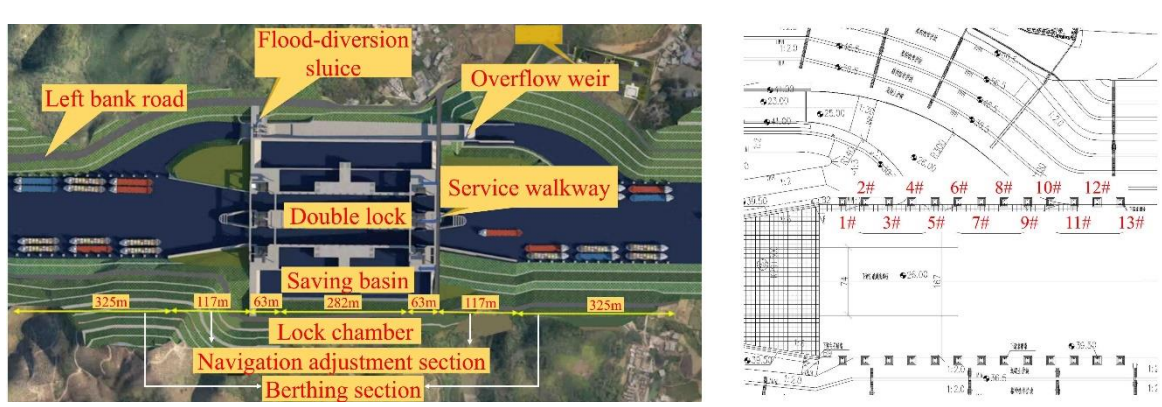


Fig. 2 Layout of Madao hub (overhead photograph (left) and definition of pier numbers (right))

characteristics of ship-berthing piers under oblique flow conditions. The interactions between the fluid and structure were simulated using the FEM, with force and displacement information exchanged between the fluid and the solid piers. This approach captured key coupling effects, such as the pressure distribution, drag forces, and fluid-induced loads on the piers.

3. METHODOLOGY

The Reynolds-averaged Navier–Stokes (RANS) equations with the renormalization group (RNG) k-ε turbulence model and the FSI model were employed to simulate and analyze the flow and force characteristics of piers under oblique water flow impact. The model was validated by experimental test data.

3.1 Fluid-Structure Interaction Model and Governing Equations

The FSI model resolved the elastic stress fields within the solid components through fully coupled solid–fluid dynamics, considering the fluid as an incompressible Newtonian fluid and the solid components as elastic. Diverging from conventional finite-difference-based fluid solvers that employ finite difference grids, this model employs a conforming unstructured finite element (FE)

discretization method to achieve higher resolution of the structural stress distributions and deformation patterns. During preprocessing, an FE mesh was generated via Cartesian grid extrusion around the solid domain to solve the governing equations of structural motion. Solid domain stresses were computed using the generalized minimal residual (GMRES) method, which iteratively minimized the residual norm. The solution procedure encompassed four concurrent processes:

- (1) Fluid domain computation (pressure and shear stress evaluation)
- (2) Hydrodynamic load transfer to the fluid-solid interface
- (3) FE analysis of the solid domain (updating displacement and stress fields)
- (4) Dynamic mesh adaptation (including hexahedral/tetrahedral element deformation or local remeshing). Ultimately, a strongly coupled iterative scheme was used to achieve displacement—load equilibrium at the fluid—solid interface.

1. Hydrodynamic Mathematical Model

The three-dimensional computational simulations in this study were conducted using the commercial CFD

software FLOW-3D. The turbulence effects were modeled by the RNG k- ϵ turbulence model. The governing equations are as follows:

Continuity Equation (Mass Conservation):

$$\frac{\partial \rho}{\partial t} + \frac{\partial (\rho u_i)}{\partial x_i} = 0 \quad (i = 1, 2, 3), \tag{1}$$

RANS Equations (Momentum Conservation):

$$\frac{\partial(\rho u_i)}{\partial t} + \frac{\partial(\rho u_i u_j)}{\partial x_j},$$

$$= -\frac{\partial P}{\partial x_i} + \frac{\partial}{\partial x_j} \left(\mu \frac{\partial u_i}{\partial x_j} - \rho u_i' u_j' \right) + S_i,$$
(2)

where ρ is the fluid density, P is the modified pressure, u_i denotes the time-averaged velocity components in the x, y, and z directions, $\rho u_i'u_j'$ represents the Reynolds stresses, S_i is the generalized source term, and μ is the dynamic viscosity of the fluid.

The turbulent kinetic energy and dissipation rate equations are as follows:

$$\begin{split} \frac{\partial k_{T}}{\partial t} + \frac{1}{V_{F}} & \left\{ u A_{x} \frac{\partial k_{T}}{\partial x} + v A_{y} \frac{\partial k_{T}}{\partial y} + w A_{z} \frac{\partial k_{T}}{\partial z} \right\}, \\ & = P_{T} + G_{T} + DIf f_{k_{T}} - \varepsilon_{T} \end{split}$$

$$\frac{\partial \varepsilon_{T}}{\partial t} + \frac{1}{V_{F}} & \left\{ u A_{x} \frac{\partial \varepsilon_{T}}{\partial x} + v A_{y} \frac{\partial \varepsilon_{T}}{\partial y} + w A_{z} \frac{\partial \varepsilon_{T}}{\partial z} \right\} = \\ & \frac{CDIS1 \cdot \varepsilon_{T}}{k_{T}} \left(P_{T} + CDIS3 \cdot G_{T} \right) + DIf f_{\varepsilon} + CDIS2 \frac{\varepsilon_{T}^{2}}{k_{T}}, \tag{4} \end{split}$$

where k_T denotes the turbulent kinetic energy, V_F represents the fluid volume fraction, A_x , A_y , and A_z denote the components of the fluid volume fraction in the x, y, and z directions, respectively, and P_T represents the production term of turbulent kinetic energy.

2. Fluid-Structure Interaction Model

The standard equations of motion for the solid domain in the FSI model are given by

$$\rho \frac{\partial^2 X}{\partial t^2} = \nabla \cdot \sigma + \rho b,\tag{5}$$

where ρ is the density of the solid material, t is time, X is the displacement of a point within the solid material, σ is the Cauchy stress tensor, and b represents the body forces. The Cauchy stress tensor is a measure of the state of stress within a material. For an elastic solid, it is related to the material's strain, as well as the thermal stresses and other internal stresses. Strain is a measure of the physical deformation experienced by the material.

The FEM employs the weighted residual method to solve the aforementioned equations, with the weighted residual form given by

$$\begin{split} \int_{\varOmega} \Psi \left[\nabla \cdot \sigma^{n+1} + \rho b - \rho \left(\frac{x^{n+1} - 2x^n + x^{n-1}}{\Delta t^{n+1} \Delta t^n} \right) \right] d\Omega \\ &= 0, \end{split}$$

where Ψ denotes the weighting function, and Ω represents the domain of definition. The integral was numerically evaluated using Gaussian quadrature. The resulting system of linear equations was solved iteratively using the GMRES solver, similar to the approach used for solving the coupled momentum and continuity equations in fluid dynamics. The standard equations of motion were solved using the FEM.

In the FSI method, the boundary conditions on the surfaces of each element of the solid component are automatically determined by the FSI model. When these surfaces are in contact with the fluid domain, the local fluid pressure dictates the traction term $(n \sigma^{n+1})$ in the equation. Therefore,

$$n \cdot \sigma^{n+1} = -n\rho_{fluid}.\tag{7}$$

The negative sign appears because, by convention in solid mechanics, compression is defined as negative. When a boundary surface is adjacent to the fluid domain, the boundary type determines the conditions imposed on the solid. For adjacent wall boundaries, the solid domain remains fixed, meaning nodes attached to the boundary are immobile. At symmetry boundaries, nodes can slide freely along the boundary but cannot penetrate or detach from it. For other boundaries, traction is computed using the pressure from adjacent boundary elements, as defined by the governing equation. In FSI simulations, if the default coupling option ("No coupling") is selected, the interface is assumed to be fixed when an FSI component contacts another component (either standard or FSI). In this case, interface nodes remain stationary throughout the simulation.

3.2 Mesh Generation and Material Properties

In the simulation of the FSIs between piers and water flow, the mesh precision and number of elements are key factors influencing both the numerical accuracy and the computational efficiency. To accurately capture the detailed features of ship-berthing piers, a sufficiently refined mesh is required. However, this inevitably increases the number of mesh elements, significantly impacting the computational efficiency. To optimize the simulation time, the three-dimensional modeling primarily focused on the region downstream of the ship-berthing pier. The simulation domain included a spillway weir and stilling basin section, a downstream navigation channel section, and a downstream flow adjustment section.

A hexahedral structured mesh was used throughout the domain. To ensure simulation accuracy, all elements were arranged in an adjacent boundary configuration in space. Following computational mechanics best practices, grid division maintained adjacent element size ratios of $\leq 1:2$, and the cell aspect ratios were optimized to $\approx 1:1$. Critical zones (e.g., boundary layers and vortex shedding regions) utilized refined meshes with 1-m isotropic elements, whereas peripheral domains contained 2-m elements. The total number of grid elements was approximately 3.9 million.

The interactions between the water flow and the pier formed a two-way FSI problem, where the high-speed

(6)

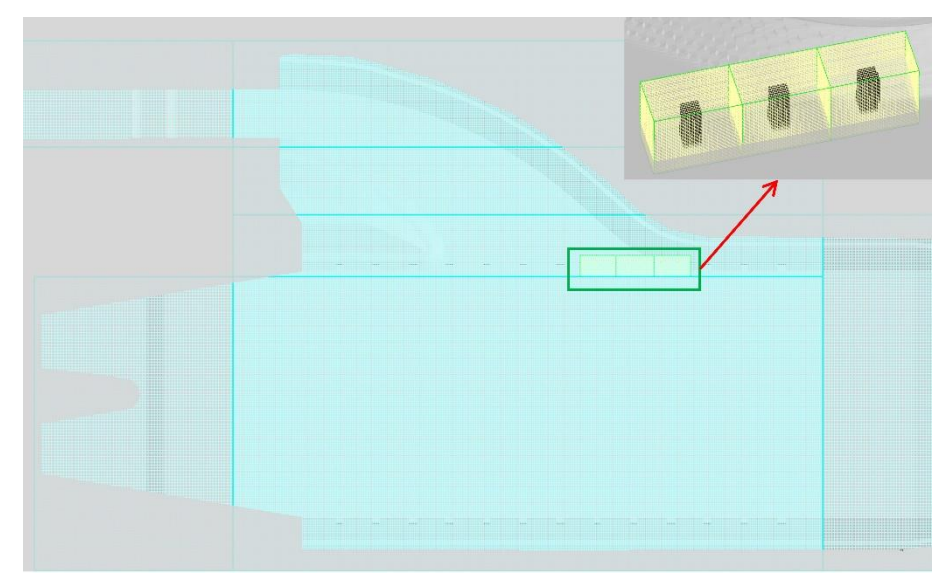


Fig. 3 Schematic diagram of mesh generation

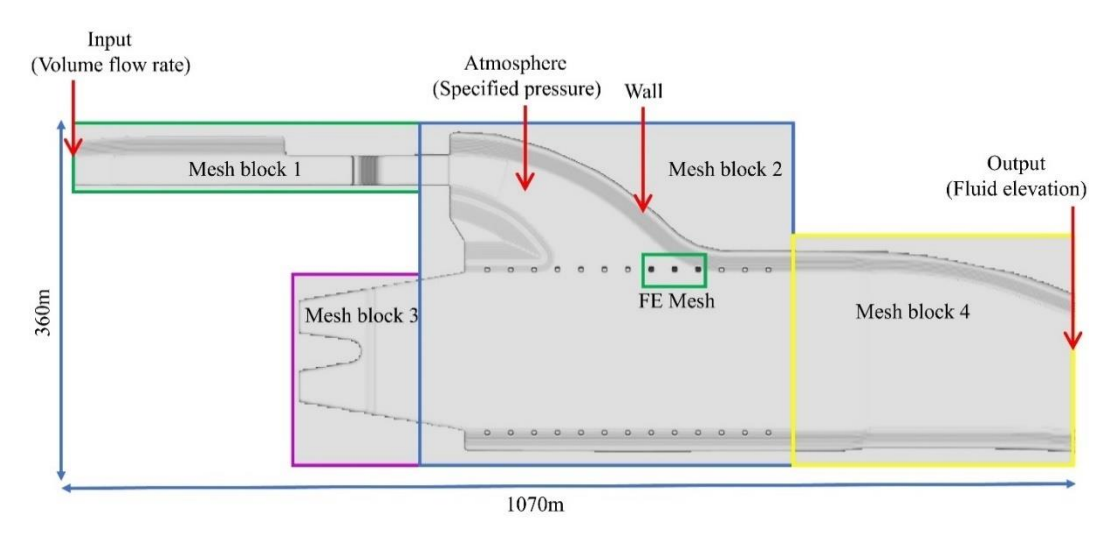


Fig. 4 Setup of boundary conditions for mathematical model

flow deformed the pier, altering the surrounding flow field and pressure distribution. As shown in Fig. 3, the FSI mesh was nested within mesh block 2, specifically around the downstream ship-berthing pier. This finer mesh had an element size of 0.5 m and contained approximately 1.2 million elements. Solid components involved in the FSIs were imported separately as regular components, and FSIs were explicitly enabled in the component properties. Additionally, material properties such as solid density, Young's modulus, and Poisson's ratio were specified accordingly.

3.3 Boundary and Initial Conditions

During a numerical simulation, the accuracy of the results is significantly influenced by the boundary and initial conditions of the computational domain. In this

simulation, different boundary conditions were applied to various regions to ensure realistic flow behavior. The inlet boundary was assigned a flow rate condition, with discharge values specified under different flood diversion scenarios. The outlet boundary was set as a pressure boundary, where the controlled water level elevation and surface pressure (atmospheric pressure) were defined. Since the upper surface of the computational domain represented the water-air interface, it was also assigned a pressure boundary with the atmospheric pressure. Within the flow channel, solid wall boundaries were imposed to constrain the fluid motion. At the start of the simulation, the initial fluid state was determined based on the downstream water level. The fluid was assumed to be static initially and followed a hydrostatic pressure distribution (see Fig. 4). Detailed operating conditions for the model are listed in Table 1.

Table 1 Simulation scenarios

Operating condition	Case1	Case 2	Case 3	Case 4	Case 5
Discharge Q (m ³ /s)	1000	1150	1300	1450	1600
Outlet water level (m)	36.32	36.76	37.19	37.63	38.06

4. VALIDATION AND ANALYSIS

To verify the appropriateness of the mesh configuration and the accuracy of the numerical results, a grid sensitivity analysis was conducted for the refined region around piers 8#, 9#, and 10#. Three mesh resolutions were tested, with minimum grid sizes of 0.8, 1.0, and 1.2 m, respectively. Under a simulated discharge of Q = 1600 m³/s and the level was fixed at 38.06 m, the velocity and pressure at both the upstream impact corner and the downstream wake corner of Pier 9# were evaluated at an elevation of Z = 35 m.

As shown in Table 2, the improvements in the accuracy diminished as the mesh became finer, and the overall numerical error was already low. Furthermore, the total number of mesh elements increased significantly with the finer resolution—3.9 million for the 1.0 m mesh versus 5.18 million for the 0.8 m mesh. Further grid refinement would substantially increase the computational cost while yielding only marginal gains in accuracy. Therefore, a minimum grid size of 1.0 m was selected for mesh refinement in the vicinity of the key piers.

To validate the accuracy of the mathematical model, a physical model test was conducted using a geometrically scaled normal model with a scale ratio of 1:60 (see Fig. 5). The validation was performed for a discharge of 1600 m³/s and a tailgate-controlled water level of 38.06 m. The comparison focused primarily on the water surface elevation and the velocity distribution. The results showed that the maximum deviation in the downstream water level was 0.06 m (see Fig. 6), which was well within the permissible limit of 0.1 m specified by relevant design standards.

Despite slight overestimations by the mathematical model, the overall velocity distribution trend aligned well with the physical model results (see Fig. 7). The primary reason for the higher velocity values in the mathematical model was the influence of high

Reynolds number turbulence, characterized by a strong outflow velocity and intense turbulent pulsations. In the physical model, flow pulsations caused fluctuations in the flow direction and velocity over time, leading to slightly lower measured values. Conversely, the mathematical model relied on the Reynolds-averaged Navier—Stokes (RANS) equations, which inherently yield higher predicted velocities than the corresponding measured values.



Fig. 5 Physical hydraulic model of Madao hub

5. RESULTS AND ANALYSIS

5.1 Flow Field Distributions Around Piers

This study primarily investigated the FSI effects on the downstream navigation pier under the impact of the downstream flow. As the flow encountered the pier obstruction, the velocity gradually decreased to zero, and the kinetic energy was gradually converted into pressure energy (deceleration and pressure increase). Subsequently, the water flow redistributed this pressure energy, converting part of it back into kinetic energy, altering its direction and accelerating along the pier's sides (acceleration and pressure decrease). Due to the water viscosity, energy dissipation occurred as the flow moved around the pier, leading to flow separation and the formation of recirculation vortices behind the pier—a

Minimum mesh size (m)	Flow velocity at impact corner point (m/s)	Flow velocity at wake region corner point (m/s)	Pressure at impact corner point (Pa)	Pressure at wake region corner point (Pa)
0.8	1.728	0.392	36984	29459
1	1.724	0.388	37199	29282
1.2	1 712	0.379	37457	29047

Table 2 Mesh sensitivity analysis results for pier 9#

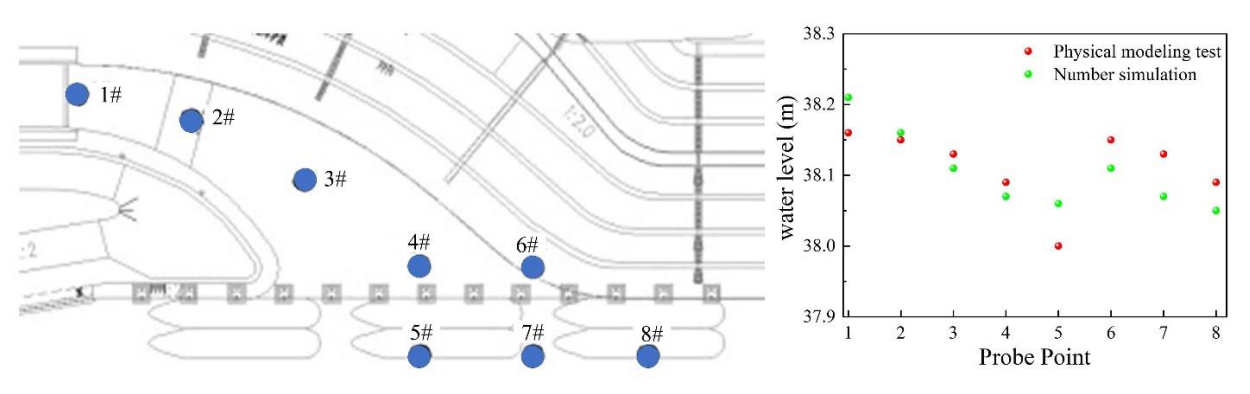


Fig. 6 Comparative analysis of downstream water levels

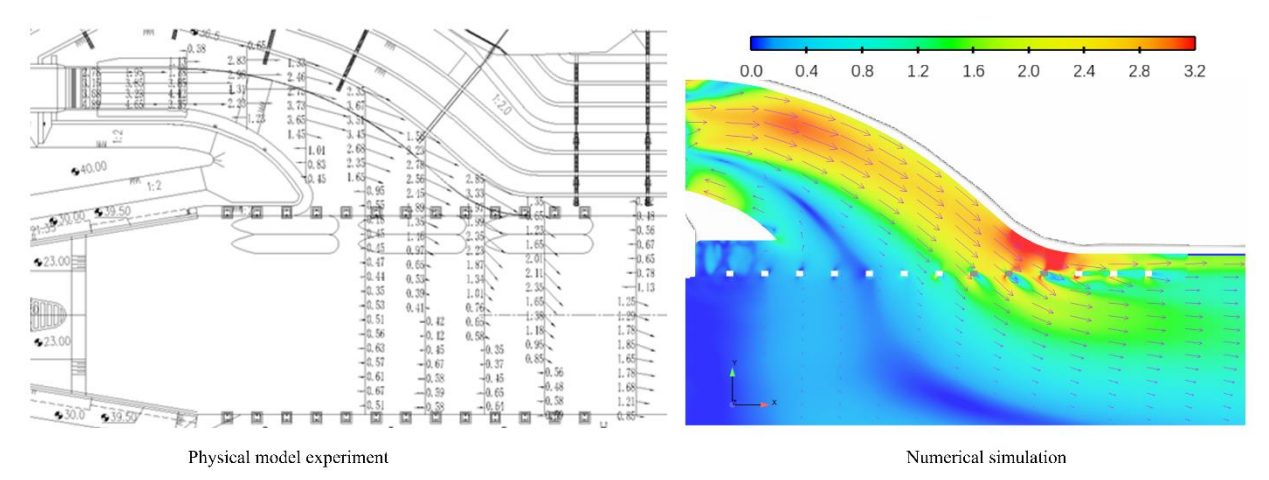


Fig. 7 Comparative Validation of Simulated and Experimental Flow Fields

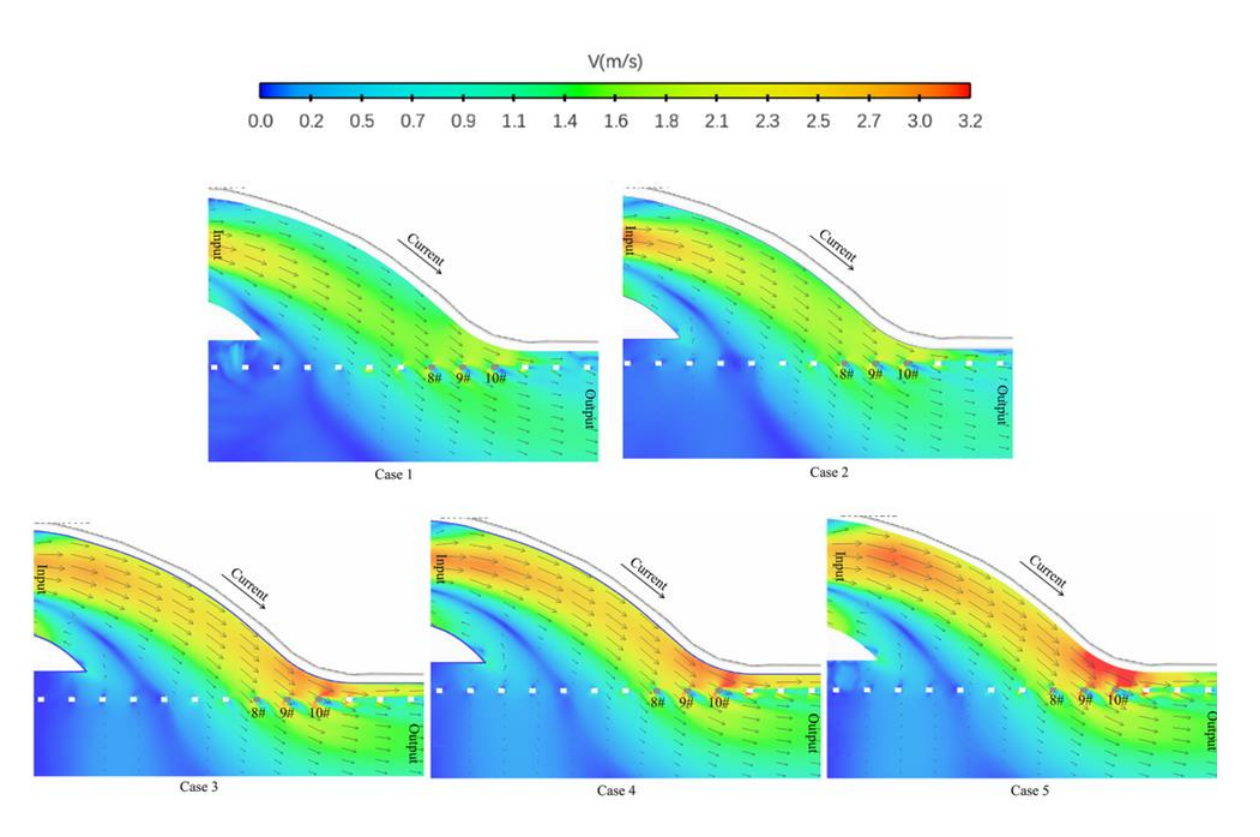


Fig. 8 Flow field distributions under various working conditions obtained by simulations

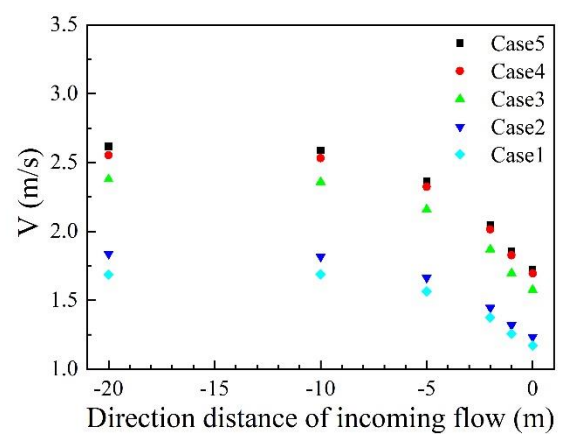
typical Kármán vortex street. These vortices gradually dissipated as they moved downstream. Consequently, a high-pressure zone formed on the upstream face of the pier, while a low-pressure zone developed on the downstream face. The resulting pressure difference between the front and back of the pier generated an impact pressure from the downstream flow. In the cross-flow direction, water accelerated along the pier's sides.

Due to the boundary conditions, the flow and pressure fields on either side of the pier exhibited asymmetry, creating a cross-flow impact pressure. After passing through the stilling basin downstream of the spillway, the discharged flow remained highly turbulent, resulting in an uneven velocity distribution across the cross section. The high-speed flow primarily followed the left bank, discharging through the flood diversion outlet,

significantly impacting piers 8# to 10#, as shown in Fig. 8

As shown in Fig. 9, the velocity of the incoming flow remained relatively stable in the region from 20 to 5 m upstream of the pier across all conditions. As the flow rate increased, the velocity gradually rose, with the most significant increase observed in Case 3, where it increased by 0.5 m/s. However, within the region from 5 m upstream to the pier itself, the velocity exhibited a sharp decline due to the obstruction posed by the pier.

In the wake region, within 20 m downstream of the pier, the flow velocity gradually increased due to the influence of the pier on the incoming flow. Beyond this distance, the velocity stabilized. Additionally, in Case 5, the velocity along the pier's surface was lower than that in



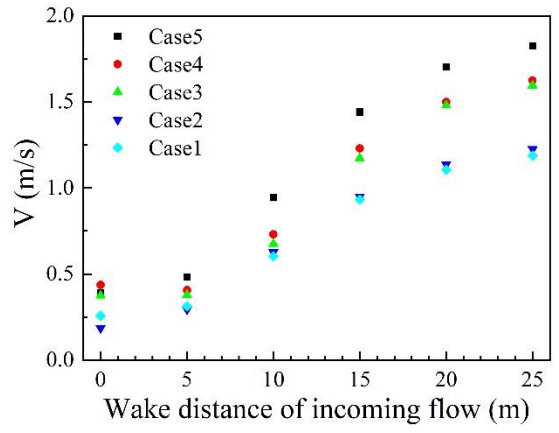


Fig. 9 Flow velocity distributions in water flow direction

Case 4, primarily because the higher flow rate altered the flow characteristics, increasing the turbulence intensity. The presence of turbulence led to velocity fluctuations in localized regions, causing fluid energy diffusion and a reduction in the velocity, which in turn generated low-speed recirculation zones. Nevertheless, it remains evident that as the flow rate increased, the velocity consistently rose, with the most pronounced increase still occurring in Case 3.

5.2 Characteristics of Pressure Distributions on Piers

The water pressure and shear stress induced by the water flow impact could lead to fatigue failure, deformation, or even structural collapse. Shear stress can cause localized surface damage and accelerate corrosion, while water pressure influences the overall structural stress distribution. Additionally, when water flow impacts vessels, shear stress increases the surface friction, affecting both the navigation stability maneuverability. Therefore, both structural and vessel design must account for the dynamic response to the water flow impact, incorporating reinforcement strategies and optimized structural configurations to ensure safe operation under complex flow conditions.

1. Analysis of Horizontal Pressure Distribution Characteristics

To assess the force distribution exerted by the water flow on the ship-berthing pier, we focused on the primary impact zones, specifically piers 8#, 9#, and 10#. Of these piers, pier 9# experienced the greatest impact force across the five conditions, making it the primary subject of this analysis. The corner of pier 9# impacted by the water flow was selected as the reference point (zero point), and a total of 20 measurement points were arranged around the pier (see Fig. 10).

During flood diversion at the Madao Hub, the spillway outflow forms a hydraulic jump within the stilling basin, generating highly turbulent flow. This turbulence consists of vortices of varying sizes and rotational directions, causing intense mixing and fluctuations in both the flow velocity and pressure. In the present simulation, a steady inflow process was modeled, with piers positioned at the intersection between the discharge channel and the downstream river. This location was characterized by a sharp bend and rapid flow

variation, leading to strong turbulence, significant wave surges, and substantial water level differences between the upstream and downstream sides of the pier. The water pressure distributions at different heights along the upstream face of the pier were obtained from the simulations. The pressure distribution contours around the pier are shown in Fig. 8. The highest water pressure was concentrated at the leading corner impacted by the flow, with pressure gradually diminished along the sides. The densely packed contour lines near the side corners indicated that sharp pressure variations occurred, while on the downstream side (wake direction), the contour lines converged rapidly, signaling intense pressure fluctuations and the presence of recirculation zones.

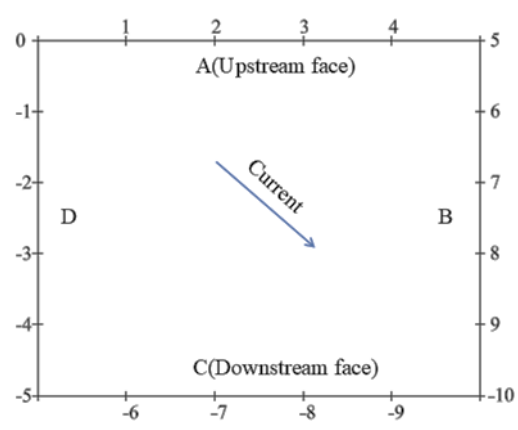


Fig. 10 Layout of horizontal measurement points

As shown in Fig. 11, the water pressure distributions on the surfaces of pier 9# exhibited a consistent overall trend at various depths. However, the pressure fluctuation amplitudes were relatively large, indicating a harsh hydrodynamic environment around the pier. To further analyze the horizontal distribution of the water pressure, we selected two representative heights for comparison: 1/3 of the pier height (Z = 30 m) and 2/3 of the pier height (Z = 35 m) (see Fig. 12).

Various conditions were considered. At Z = 30 m, the water pressure ranged from 57,000 to 85,000 Pa. At Z = 35 m, the water pressure ranged from 10,000 to 37,000 Pa. Across all scenarios, the water pressure on the downstream side initially decreased gradually, followed by a gradual increase. On the upstream side, the pressure

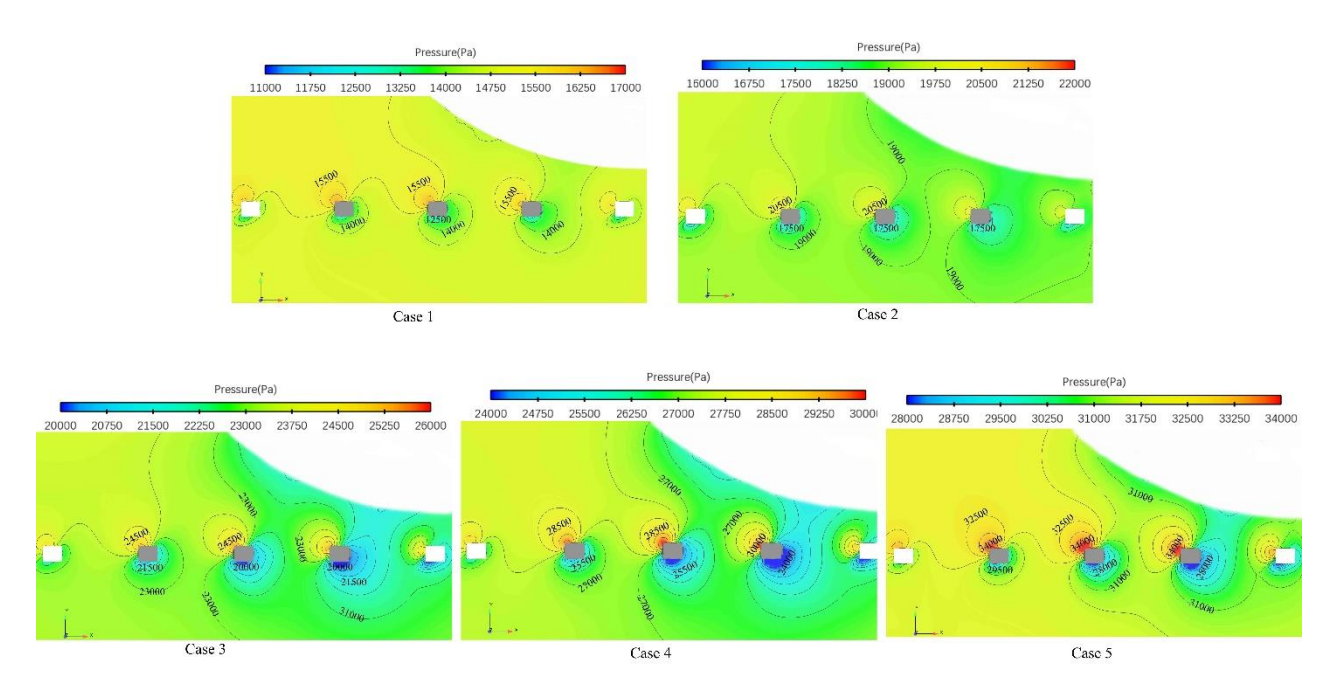


Fig. 11 Pressure field distributions at Z = 35 m

rose sharply, reaching its peak near the leading corner impacted by the flow. This was primarily due to the direct and intense impact of the incoming flow on this face. Beyond this impact point, the pressure dropped rapidly but remained higher than that on the other three sides. On the downstream side, the pressure first underwent a brief decline, followed by a gradual increase, influenced by the wake flow dynamics. These variations highlighted the complex interactions between the pier structure and the turbulent flow field.

2. Analysis of Vertical Pressure Distribution Characteristics

At a flow rate of $Q = 1600 \text{ m}^3/\text{s}$ and a downstream controlled water level of 38.06 m, the transient total pressure distributions around piers 8#, 9#, and 10# at t = 2000 s are shown in Fig. 13. The results indicated that the water pressure gradually increased with depth, consistent with the hydrostatic pressure principle. The simulation replicated the actual flow conditions, where the water surface remained a free liquid surface and the space above it was occupied by gas. As water flowed past the pier, it accumulated upstream, causing a noticeable rise in the water surface, reaching its peak at the front edge of the pier.

The forces acting on the pier resulted from both the dynamic pressure from the flow field and the static pressure from the water depth. Consequently, the stress values increased toward the bottom of the pier due to the greater hydrostatic pressure. Conversely, in the upper region, the static pressure was lower, exerting a weaker influence on the pier structure. This led to consistent variations in both the force and pressure along the pier. The water pressures at the measurement points on each ship-berthing pier followed a gradual increase from top to bottom, with pressure values closely corresponding to the water depth.

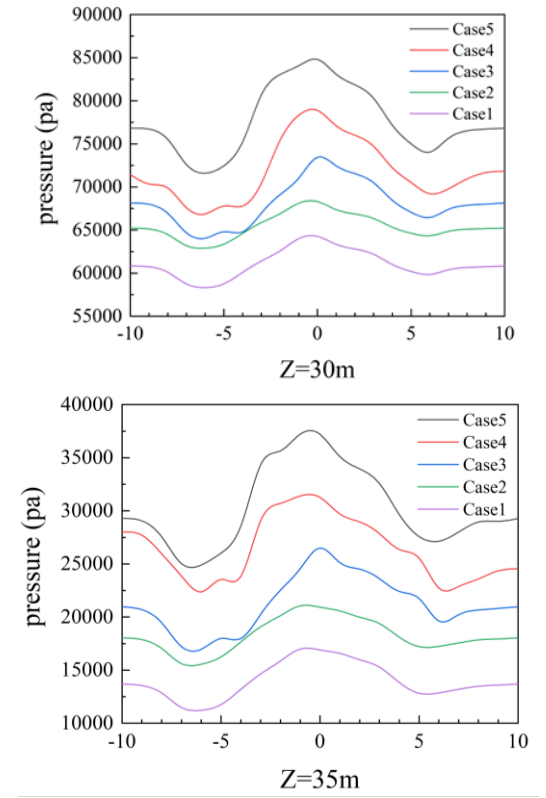


Fig. 12 Horizontal pressure of pier 9# under various working conditions

To quantitatively analyze the vertical distribution of the water pressure, five horizontal cross sections were selected at water depths of 2, 4, 6, 8, and 10 m on the shipberthing pier. Fig. 14 shows the arrangement of measurement points at each cross section. Pier 9# was selected to examine water pressure distribution patterns under various conditions.

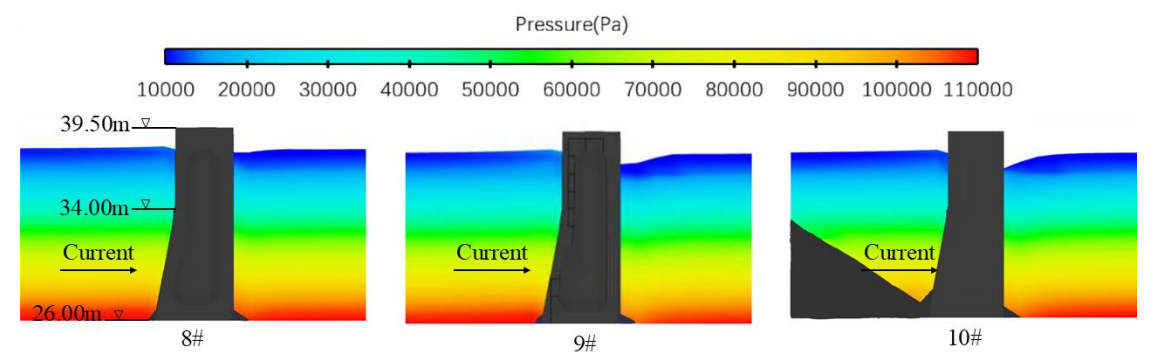


Fig. 13 Local pressure fields of berthing piers

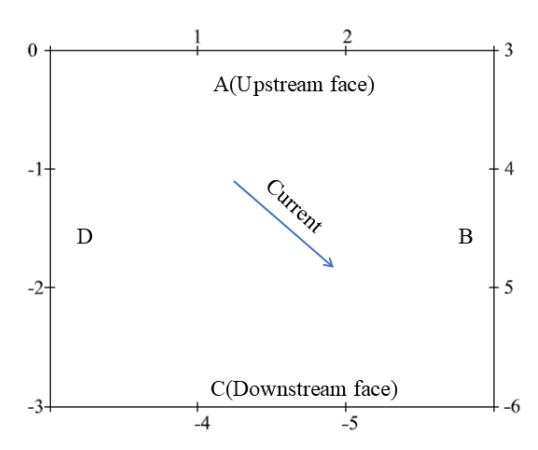


Fig. 14 Layout of horizontal measurement points

Based on the pressure distribution around each shipberthing pier, after the computation stabilized at t = 2000s, the dynamic water pressure distribution patterns were similar across all conditions. The maximum value of -25,000 Pa was recorded at a water depth of 10 m, The minimum value was observed at a water depth of 4 m, where the pressure fluctuated around zero. On Side A (measurement points 0 to 2), although the dynamic water pressure decreased, it remained relatively high, with significant pressure fluctuations. In the vertical direction, the pressure first decreased and then increased between 2 and 4 m, and similarly between 6 and 8 m. A continuous increase was observed from 8 to 10 m, culminating in a negative dynamic water pressure (see Fig. 15). On Side B (measurement points 3 to 5), the variation in the dynamic water pressure with the depth was more gradual compared to the variations on the other sides (see Fig. 16). On Side C (measurement points -6 to -4), the pressure fluctuations were relatively stable between points -6 and -5, while significant fluctuations occurred between points -5 and -4. This was primarily due to the water flow impacting the pier, which obstructed the flow and caused a substantial drop in the water level between points -5 and -4, thereby exacerbating the pressure fluctuations (see Fig. 17). On Side D (measurement points -3 to -1), the entire pier surface experienced intense pressure fluctuations at all water depths. This side was the main impact surface, influenced by the flowing water, resulting in significant water level fluctuations and the phenomenon of water accumulation in front of the pier (see Fig. 18).

Overall, the primary force-bearing surfaces of the pier under the impact of the water flow were the upstream side

and the front face (side D). The dynamic water pressure on the upstream side was generally higher, reaching a maximum negative pressure of 25,000 Pa. The negative value of the dynamic water pressure indicated a state of negative pressure. The negative pressure effect of the water flow could cause a tilting force on the pier in the direction of the water flow, increasing the risk of pier overturning. Additionally, the negative pressure altered the force distribution on the pier, causing uneven loading and increasing the force in the direction of the water flow, thereby affecting the overall load-bearing performance of the pier. Moreover, the negative pressure increased the suction force of the water flow on the pier surface, and accelerating corrosion, thus reducing the service life of the ship-berthing pier. Lastly, under the influence of the water flow, local cavitation may occur behind the pier, increasing the surrounding water flow velocity and enhancing the impact force, which in turn would affect the structural stability of the pier.

5.3 Distribution Patterns of Water Flow Impact Forces

To analyze the distribution of the water flow impact forces, relevant engineering standards, including the Australian Standard (AS 5100), the Indian Roads Congress (IRC 6), and the Indian Railways Standards (IRS), were reviewed (Patil & Kadam, 2024a). The study highlights the necessity of incorporating FSI effects in bridge pier designs subjected to oblique water flow. The results of the FSI analysis, as shown in Fig. 19, demonstrated strong consistency with both the AS 5100 standard and the IRS guidelines, validating their applicability under specific hydraulic conditions. However, when applying the IRC 6 standard for structural design, significant discrepancies emerged between the simulation results and the recommended values from the standard. This deviation underscores the need for a dynamic evaluation mechanism, incorporating parameter adjustments or multi-scale coupling analysis, to ensure the reliability and compliance of the design schemes.

Based on the Madao Hub project of the Pinglu Canal, a three-dimensional FSI model was developed in this study to systematically compare the distribution characteristics of the water pressure under flood discharge conditions with those obtained from the AS 5100, IRC 6, and IRS standards. By integrating simulation technology with standard-based frameworks, the nonlinear coupling mechanism between the transient water pressure pulsations

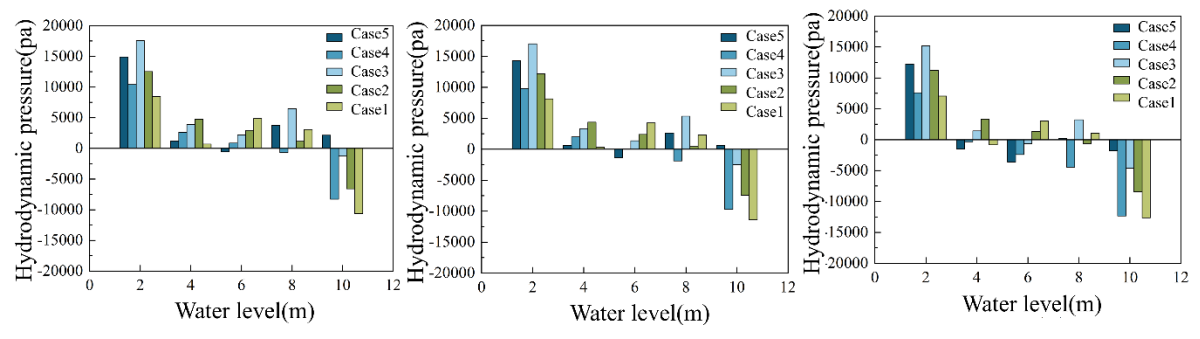


Fig. 15 Vertical pressure distribution on side A

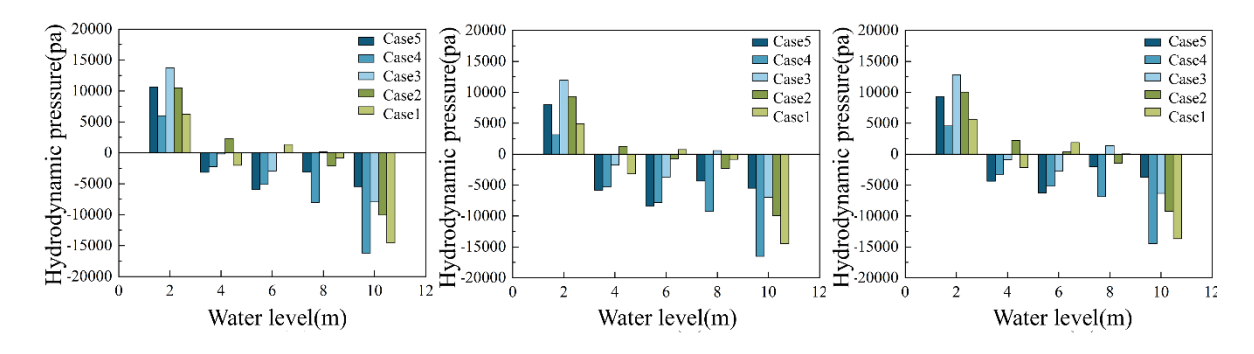


Fig. 16 Vertical pressure distribution on side B

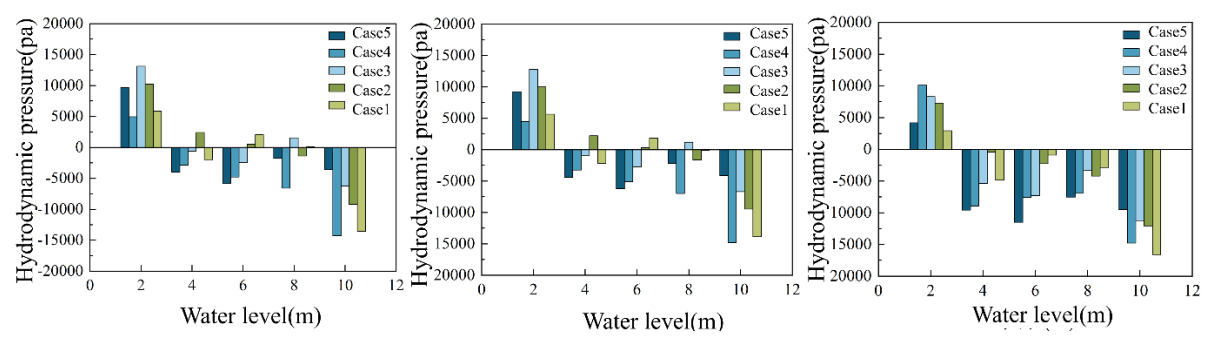


Fig. 17 Vertical pressure distribution on side C

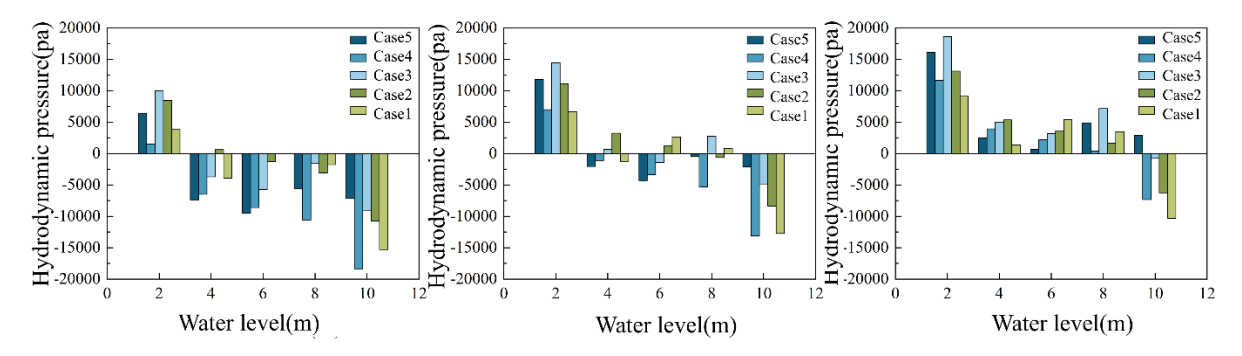


Fig. 18 Vertical pressure distribution on side D

and the structural dynamic responses was revealed. The findings indicated that under extreme hydraulic gradients, the prediction deviations of IRC 6 could reach up to 85%, as shown in Fig. 19.

The discrepancy between the simulation and IRC 6 predictions can be explained by two key factors:

1) IRC 6 is based on a static load hypothesis. The constant in its formula represents an empirically bundled quantity based on the fluid density and gravitational

acceleration, failing to explicitly reflect the other fluid properties. Furthermore, this formula completely neglects the dynamic coupling effects of FSIs, resulting in systematic deviations between the calculated pressure distribution and the FSI simulation results. Such a simplified model cannot capture the vortex-induced vibrations triggered by flow separation, constituting a theoretical limitation.

2) When the flow velocity exceeded 2 m/s, IRC 6 exhibited significantly increased errors. The fundamental

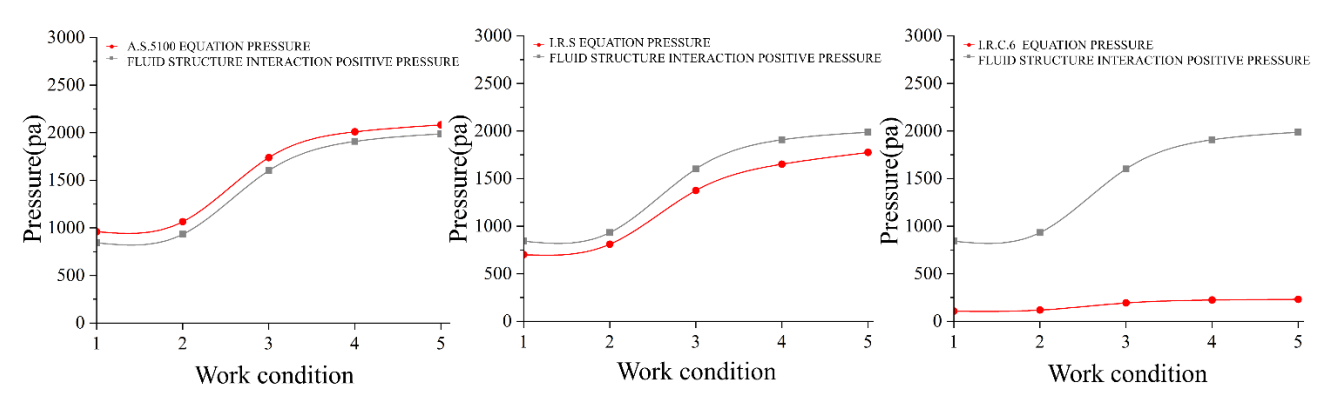


Fig. 19 Comparison of fluid-structure interaction analysis results and predictions obtained from standards

reason for this discrepancy was the dominance of the fluid inertial forces under high-velocity flow conditions, where the FSI effects intensified the pier vibrations. However, IRC 6's static model could not account for this dynamic amplification effect. Consequently, the design predictions based on IRC 6 are no longer conservative at high speeds, potentially compromising pier safety. Through cross-validation of multi-physics data, this research provides a theoretical foundation for the engineering application of different standard systems and can be used to establish a bridge pier safety assessment matrix based on risk coefficients.

6. CONCLUSIONS

In this study, five different scenarios under oblique water flow were simulated using an FSI model to analyze the coupling effects of downstream flow on ship-berthing piers. The forces on the pier surfaces were computed using a GMRES solver combined with an explicit coupling algorithm, and the results were validated against empirical formula predictions. The consistency between the simulations and theoretical results confirmed the reliability of the two-way coupling method in capturing the interactions between piers and water flow.

- 1. After passing through the stilling basin downstream of the spillway, the water flow primarily descended along the left bank and was discharged through the flood diversion outlet. Under maximum discharge conditions, the mainstream velocity ranged from 1.8 to 3.8 m/s, exerting the most significant impact on piers 8# to 10# in the downstream navigation channel, with pier #9 experiencing the highest forces. The simulations effectively captured the free liquid surface characteristics and the accumulation of water in front of the pier, accurately reflecting the real flow conditions.
- 2. Upon oblique impact with the high-speed downstream flow, the ship-berthing pier developed distinct pressure zones. A positive pressure region formed on the upstream face and side, while a negative pressure zone appeared on the downstream face and side. The highest positive pressure was concentrated near the corner of the pier directly impacted by the flow, whereas the maximum negative pressure was located on the downstream face. As the water flowed over the apex of the upstream face and moved toward the side walls, it

gradually separated from the surface, causing a reduction in the hydrodynamic pressure. This pressure dropped to negative values at the right end of the upstream face and on the downstream end of the upstream side, leading to the formation of a horseshoe vortex region in the downstream negative pressure zone.

3. A comparison with engineering standards revealed that the AS 5100 and IRS guidelines aligned well with the FSI analysis results under conventional hydraulic conditions, whereas the IRC 6 standard exhibited systematic deviations when predicting forces in high-speed oblique flow fields. To address these discrepancies, a zonal correction factor based on the flow characteristics should be introduced, along with a dynamic probabilistic design approach. By stochastically coupling FSI time-history analysis results with standard limit states, a refined assessment framework can be developed to achieve a balance between structural safety and economic feasibility.

This study focused mainly on the hydraulic responses under short-term flow regimes, which induced relatively minor effects on the pier columns. Subsequent research will delve into the cumulative scour effects and structural responses under long-term flow conditions, which are the key refinement objectives of our research team.

ACKNOWLEDGEMENTS

This work was supported by the National Natural Science Foundation of China (grant number 52109150), Natural Science Foundation of Chongqing (grant number CSTB2023 NSCQ-MSX0767), and Key Laboratory of Inland Waterway Regulation Engineering of the Ministry of Communications, Chongqing Jiaotong University (No. KLIWRE2023B01). We thank LetPub (www.letpub.com.cn) for linguistic assistance and presubmission expert review.

CONFLICTS OF INTEREST

The authors have no conflicts of interest to disclose.

AUTHOR CONTRIBUTIONS

Yan Li and Yuanyuan Li contributed equally to this work and should be considered co-first authors. Yan Li:

Conceptualization, Software, Validation. Yuanyuan Li: Writing—original draft, Resources, Supervision. Qian Ma: Formal analysis, Writing—review & editing, Funding acquisition. Pengyu Zhou: Investigation, Supervision. Chaozhe Zhang: Investigation. Xiaoshuang Cheng: Data curation.

REFERENCES

- Baduna Koçyiğit, M., & Koçyiğit, Ö. (2024). Experimental Investigation of Bridge Scour under Pressure Flow Conditions. *Water*, *16*(19), 2773. https://doi.org/10.3390/w16192773
- Baragamage, D. S. P. A., & Wu, W. (2024). A Three-Dimensional Fully-Coupled Fluid-Structure Model for Tsunami Loading on Coastal Bridges. *Water*, *16*(1), 189. https://doi.org/10.3390/w16010189
- Cai, Y., Ma, B., Wang, F., Fan, Y., Chang, H., Zhang, H., Wang, Y., & Zheng, Y. (2025). Structural parameters analysis and optimization design study of double-pier linkage-type anticollision device. *Ocean Engineering*, 317, 120084. https://doi.org/10.1016/j.oceaneng.2024.120084
- Cao, Y., & Tamura, T. (2018). Shear effects on flows past a square cylinder with rounded corners at Re=2.2×104. *Journal of Wind Engineering and Industrial Aerodynamics*, 174, 119–132. https://doi.org/10.1016/j.jweia.2017.12.025
- Carnacina, I., Leonardi, N., & Pagliara, S. (2019). Characteristics of Flow Structure around Cylindrical Bridge Piers in Pressure-Flow Conditions. *Water*, 11(11), 2240. https://doi.org/10.3390/w11112240
- Çelik, Z., & Altaç, Z. (2023). Numerical investigation of two-dimensional unsteady flow and heat transfer from rounded equilateral isothermal triangular cylinders in cross flow. *Ocean Engineering*, 269, 113468.
 - https://doi.org/10.1016/j.oceaneng.2022.113468
- Chen, Y., Huang, X., Wu, K., & Li, Z. X. (2025). Hydrodynamic effects and prediction of the responses of underwater rectangular bridge piers during earthquakes. *Engineering Structures*, 326, 119518.
 - https://doi.org/10.1016/j.engstruct.2024.119518
- Gao, Y., Qu, X., Zhao, M., & Wang, L. (2019). Three-dimensional numerical simulation on flow past three circular cylinders in an equilateral-triangular arrangement. *Ocean Engineering*, 189, 106375. https://doi.org/10.1016/j.oceaneng.2019.106375
- Huang, D. (2023). Numerical Simulation of the Influence of Water Flow on the Piers of a Bridge for Different Incidence Angles. *Fluid Dynamics & Materials Processing*, 19(3), 845–854. https://doi.org/10.32604/fdmp.2022.020314
- Jeong, W., & Seong, J. (2014). Comparison of effects on technical variances of computational fluid dynamics

- (CFD) software based on finite element and finite volume methods. *International Journal of Mechanical Sciences*, 78, 19–26. https://doi.org/10.1016/j.ijmecsci.2013.10.017
- Kadono, T., Okazaki, S., Kabeyama, Y., & Matsui, T. (2020). Effect of Angle between Pier and Center of River Flow on Local Scouring around the Bridge Pier. *Water*, 12(11), 3192. https://doi.org/10.3390/w12113192
- Lin, T.-K., Chen, P.-W., & Chang, H.-T. (2022). A Fluid-Structure Interaction Model for Bridge Safety Assessment under Scour Conditions. *Shock and Vibration*, 2022, 1–17. https://doi.org/10.1155/2022/2090470
- Luo, J.-L., Pei, J., Yan, Y., & Wang, W.-Q. (2022).

 Numerical study of the flow around a hyperbolic cylinder at Reynolds number 3900. *Ocean Engineering*, 246, 110669.

 https://doi.org/10.1016/j.oceaneng.2022.110669
- Nan, X., Liu, X., Chen, L., Yan, Q., & Li, J. (2023). Study of the bridge damage during flooding based on a coupled VOF-FSI method. *Journal of Engineering Research*, *11*(3), 51–61. https://doi.org/10.1016/j.jer.2023.100081
- Omara, H., Saleh, O. K., Al-Mutiry, M., Masria, A., & Tawfik, A. (2023). Assessment the local scour around vertical and inclined oblong piers under shallow flow condition. *Ocean Engineering*, 281, 114835.
 - https://doi.org/10.1016/j.oceaneng.2023.114835
- Ozdemir, Z., Souli, M., & Fahjan, Y. M. (2010). Application of nonlinear fluid–structure interaction methods to seismic analysis of anchored and unanchored tanks. *Engineering Structures*, 32(2), 409–423.
 - https://doi.org/10.1016/j.engstruct.2009.10.004
- Pang, Y., Luo, Q., Wei, K., Deng, K., & Chen, X. (2025). Seismic resilience assessment of reinforced concrete bridges constructed with tall piers in the deep-water environment. *Engineering Structures*, *325*, 119387. https://doi.org/10.1016/j.engstruct.2024.119387
- Patil, D., & Kadam, S. (2024a). Assessment of Hydrological Pressure on Concrete Bridge Piers Considering Fluid–Structure Interaction. *Journal of Performance of Constructed Facilities*, 38(6), 04024048.
 - https://doi.org/10.1061/JPCFEV.CFENG-4809
- Patil, D., & Kadam, S. (2024b). Assessment of water pressure on reinforced concrete highway bridge piers by univariate regression analysis approach. *Journal of Building Pathology and Rehabilitation*, *9*(1), 21. https://doi.org/10.1007/s41024-023-00373-4
- Rahman, H., Khan, I., Islam, S. U., Abbasi, W. S., Ullah, R., & Khan, M. U. (2022). Numerical analysis of fluid flow dynamics around two side-by-side square

- cylinders in the presence and absence of splitter plate. Journal of the Brazilian Society of Mechanical Sciences and Engineering, 44(11), 552. https://doi.org/10.1007/s40430-022-03804-4
- Sousa, P., Rodrigues, C. V., & Afonso, A. (2024). Enhancing CFD solver with Machine Learning techniques. *Computer Methods in Applied Mechanics and Engineering*, 429, 117133. https://doi.org/10.1016/j.cma.2024.117133
- Tu, J., Zhang, Z., Lv, H., Han, Z., Zhou, D., Yang, H., & Fu, S. (2020). Influence of the center cylinder on the flow characteristics of four- and five-cylinder arrays at subcritical Reynolds number. *Ocean Engineering*, 218, 108245. https://doi.org/10.1016/j.oceaneng.2020.108245
- Wang, Y., Zou, Y., Xu, L., & Luo, Z. (2015). Analysis of Water Flow Pressure on Bridge Piers considering the Impact Effect. *Mathematical Problems in Engineering*, 2015, 1–8. https://doi.org/10.1155/2015/687535
- Yang, W., Li, A., Feng, X., Deng, L., & Li, F. (2020). Calculation method of hydrodynamic force on one column of the twin columns under earthquake. *Ocean Engineering*, 197, 106874. https://doi.org/10.1016/j.oceaneng.2019.106874
- Zhao, C., & Guo, C. (2024). Investigation of the large-diameter monopiles response under flow-controlled loading. *Marine Georesources & Geotechnology*, 1–11.
 - https://doi.org/10.1080/1064119X.2024.2420908